

Structure and properties of tin-doped indium oxide thin films prepared by reactive electron-beam evaporation with a zone-confining arrangement

I. A. Rauf^{a)}

Microstructural Physics Group, Cavendish Laboratory, Madingley Road, Cambridge CB3 0HE, United Kingdom

(Received 7 February 1995; accepted for publication 15 December 1995)

The microstructure and electrical properties of tin-doped indium oxide thin films crystallized under the action of a temperature gradient are compared with those of films prepared under uniform temperature. This zone-confining process, coupled with slow deposition rates, causes preferential segregation of dopants from grains growing at lower temperatures toward grain boundaries located at higher temperature. Recrystallization within a chain or zone of grains on a line of equal temperature causes these grains to be oriented in the same direction. The boundaries separating grains are twin boundaries. Electronic mean free paths in the zone-confined specimens are from two to four times the average size of the grains. © 1996 American Institute of Physics. [S0021-8979(96)01407-4]

I. INTRODUCTION

Transparent semiconducting oxide films and techniques for their production have been investigated for many years because of their unique properties and extensive applications.¹ There is also fundamental interest in the mechanism of conduction. The association of physical properties with details of the microstructure has been the objective of much solid-state science carried out on these films. Such a quantitative correlation requires a knowledge of the crystallite size and orientation, as well as of the density of planar, linear, and point defects. In tin-doped indium oxide, tin is a substitutional dopant randomly located at indium sites. Although tin is a neighbor of indium in the periodic table, the difference in ionic radius ($\text{Sn}^{4+}=0.205$ nm, $\text{In}^{3+}=0.218$ nm) introduces a localized strain as well as a defect and charge center in the indium oxide lattice. Conduction electrons will therefore be scattered resulting in a reduction of the free carrier mobility and electrical conductivity. Other consequences of doping are

- (i) segregation of dopant atoms toward grain boundaries;¹
- (ii) cluster formation to form local concentrations of Sn_2O_3 ;²
- (iii) an intergranular amorphous phase at high dopant concentrations.³

A number of thin-film deposition techniques has been used to deposit indium tin oxide (ITO). Since the electrical and optical properties in these films depend strongly on their microstructure, stoichiometry, and the nature of the impurities which are present, each technique yields films with different behavior. A recently developed zone-confining process^{4,5} in which films are crystallized under a local temperature gradient has produced ITO films with properties which see no rival in the literature. This article compares the

microstructure of ITO films prepared under a zone-confining arrangement with that of films prepared by conventional deposition methods.

II. EXPERIMENT

A. Sample preparation

Indium oxide and tin oxide powders mixed in different proportions using a mortar and pestle were pressed to form pellets which were sintered in air at 675 °C for 24 h. The sintered pellets were electron-beam evaporated from a copper crucible in an Edwards 306 coating unit. Fused quartz slides, cleaned in an ultrasonic bath with acetone for 15 min, and freshly cleaved rocksalt substrates were loaded into the vacuum chamber which was evacuated to a base pressure of less than 5×10^{-4} Pa. Two sets of samples were prepared. First, a substrate heater was used in which a 4-mm-thick copper plate produced a uniform temperature distribution of 250 ± 3 °C over the area of the substrate. The temperature was monitored by an Alumel/Chromel thermocouple attached to the top surface of the substrate. Four specimens were prepared at a deposition rate of 4–5 nm/min, oxygen partial pressure of 0.08 Pa, and with four different concentrations of Sn in the films (i.e., 4.2, 5.1, 6.6, and 9.3 at. %). This deposition rate is much slower than the rates of 120 nm/min normally used for tin-doped indium oxide thin films.⁶ Slower deposition rates were used to allow time for atoms to diffuse during the deposition. A second set of four samples was prepared under identical condition except that the copper plate was removed to create a temperature gradient over various parts of the substrate, and the average substrate temperature was raised to 300 °C to enhance the zone-confining effect. A shutter mechanism was used to cover the rocksalt substrates while thicker films (82–1200 nm) were being deposited onto fused quartz slides for studies of the electrical and optical properties. The shutter was removed for 5 min to deposit 20–25-nm-thick films on rocksalt for electron microscopy. After completing the deposition the films were left at the same oxygen partial pressure to cool to room temperature.

^{a)}Present address: Department of Physics, Queen's University, Kingston, Ontario K7L 3N6, Canada; Electronic mail: raufi@qucdn.queensu.ca

TABLE I. Texture coefficient for different sets of planes as a function of dopant concentration C_{Sn} for the specimens prepared under normal conditions.

G_{Sn} (at. %)	No. of peaks	Texture coefficient						
		{211}	{222}	{400}	{411}	{431}	{440}	{622}
4.2	15	2.08	2.45	2.16	0.92	0.74	1.02	0.92
5.1	13	2.29	1.42	1.76	0.89	0.57	0.79	0.65
6.6	11	2.31	1.58	1.39	0.79	0.47	0.66	0.59
9.3	14	2.40	2.23	1.89	0.56	0.67	0.87	0.74

B. Sample characterization

Films deposited on rocksalt were floated off in distilled water and were transferred to holey carbon microscope grids. X-ray-diffraction experiments were performed on films deposited on fused quartz slides using a Spectrolab 3000 diffractometer with Cu $K\alpha$ radiation ($\lambda=15.41$ nm). A JEOL 2000EX transmission electron microscope (TEM) was used to study the microstructure of the specimens. Selected area electron diffraction (SAED) patterns were recorded using a 100 μm aperture. For dark-field images the strongest diffracted beam (corresponding to the {222} planes) was placed at the center of the objective aperture by tilting the illumination. High-resolution bright-field images were recorded using JEOL 2000EX and JEOL 200CX electron microscopes. The JEOL 2000EX was operated without an objective aperture to achieve the maximum possible resolution. The magnification was calibrated using a sputtered gold specimen, while the diffraction camera length for the 2000EX was calibrated using an evaporated aluminium film. The electrical resistivity ρ was measured using a Van der Pauw method.⁷ The free carrier density n was obtained using a method described elsewhere.⁸ The conduction mobility μ_c was calculated from⁶

$$\mu_c = 1/ne\rho. \quad (1)$$

III. RESULTS

A. Structure of normal specimens

The preferred orientation of a certain crystal plane (hkl) can be described in terms of its texture coefficient (TC_{hkl}). This coefficient represents the fraction of the grains that have { hkl } plane normals lying parallel to the film axis and is calculated using the relation given in Ref. 9. The texture coefficient represents the degree of anisotropy of the physical and mechanical properties and depends on the deviation from the single-crystal behavior and the extent of preferred orientation. Similarly, the full width at half-maximum b of the diffraction peak is related to the extent of order and crystallite size L ($b=\lambda/2L$ and λ is the wavelength of incident x rays). As the crystal size decreases the diffracted beam becomes more diffuse until it is lost in the general background.

Table I shows the number of diffraction peaks observed as a function of tin concentration for the series of specimens prepared with spatially uniform heating arrangements. The specimen with 6.6 at. % tin shows the lowest number of diffraction peaks. Table I also shows the texture coefficient, calculated for seven different planes, for the same series of

specimens. The specimen with 4.2 at. % tin shows the highest value of texture coefficient for {222} planes but the rest show a preferred orientation for {211} planes.

Figure 1 shows the SAED patterns from the series of specimens prepared under uniform temperature. These diffraction patterns showed the indium oxide bcc bixbyite structure as the dominant phase. A few traces of a hexagonal phase of indium oxide were also observed, however, no traces of a separate tin oxide phase were detected. The SAED pattern from the specimen with 6.6 at. % tin [Fig. 1(c)] shows two diffuse rings indicating that this specimen has the largest amount of disorder and that the material in this specimen consists of a mixture of amorphous and crystalline phases. None of the other specimens show any diffuse rings in their diffraction patterns. Figure 2 shows dark-field images of the specimens in the above series. Apart from Fig. 2(c) (tin concentration of 6.6 at. %) all the specimens show well-defined grains. The images of the specimens with dopant concentration above the solid solubility limit of tin in indium oxide (5 at. %) show some highly disordered grains

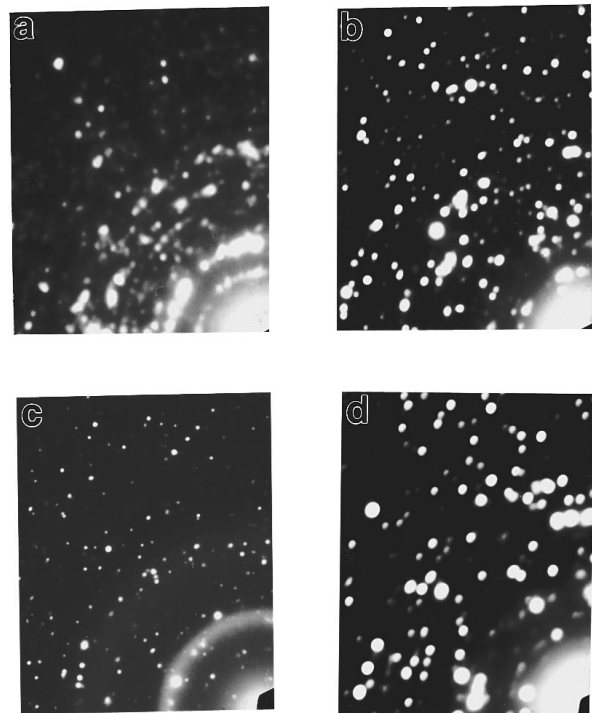


FIG. 1. SAED pattern from specimens prepared under normal conditions with dopant concentrations of (a) 4.2, (b) 5.1, (c) 6.6, and (d) 9.3 at. %.

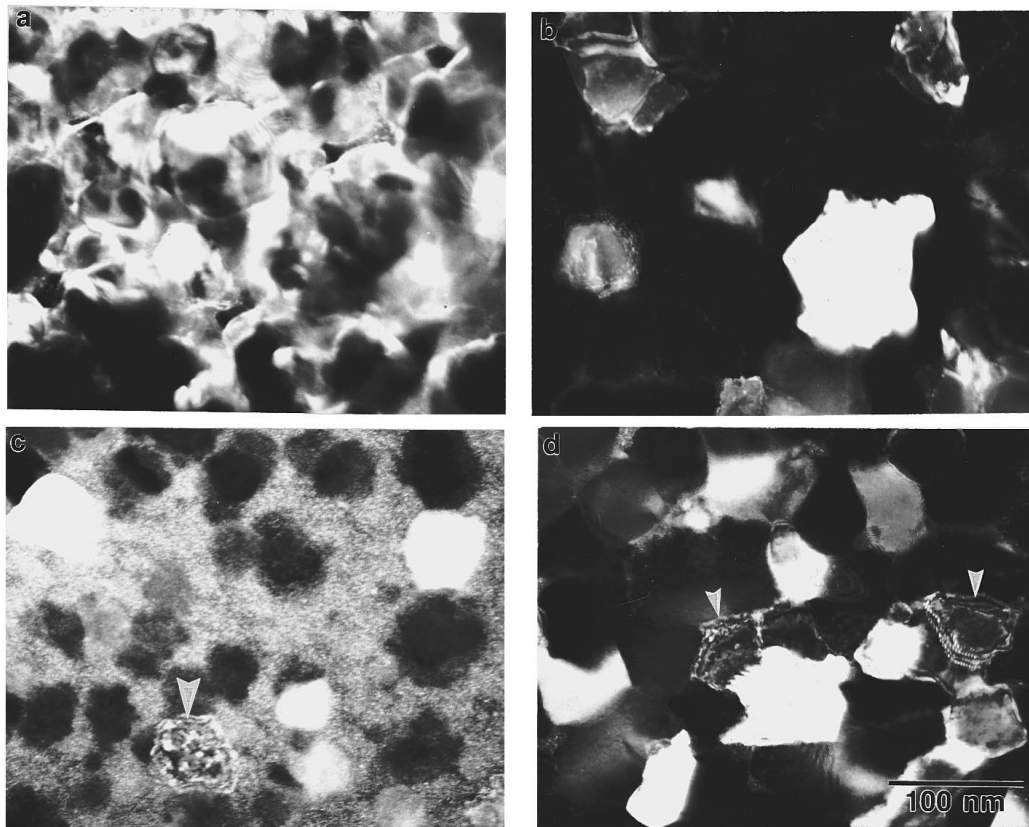


FIG. 2. Dark-field images from the specimen prepared under normal condition with a dopant concentration of (a) 4.2, (b) 5.1, (c) 6.6, and (d) 9.3 at. %.

which look as if they have been compressed or deformed. These are marked by arrows in Figs. 2(c) and 2(d).

The average grain area was calculated by counting the number of grains in a known area and dividing the total area by the number of grains. The average grain radius, assuming the grains to be two dimensional and circular, was calculated from the relation $A = \pi r^2$. Table II shows that the average grain radius decreases with increasing dopant concentration up to a tin concentration of 6.6 at. %. Above this concentration the grain size increases again and the highly disordered intergranular regions disappear. Each grain in this case is decorated with small clusters [Fig. 2(d)]. By comparing bright- and dark-field images from the same grain surface (Fig. 3) it can be seen that these clusters match each other and are brighter compared to the matrix in both type of images. This indicates that these clusters are not thickness contrast effects but might be due to the fact that the dopant atoms can no longer be accommodated in even a disordered indium oxide lattice and are hence forced to the surface of

the grain. No traces of a separate SnO_2 phase were detected in the electron-diffraction patterns from these specimens.

B. Structure of zone-confined specimens

For the specimen series prepared with a zone-confining arrangement, apart from the specimen with 4.2 at. % tin concentration, none showed any traces of a hexagonal phase in x-ray-diffraction patterns. Table III shows the number of diffraction peaks observed and the texture coefficient as a function of tin concentration. The specimen with 6.6 at. % tin again shows the lowest number of peaks in the diffraction pattern. The specimen with 6.6 at. % tin in both series has the maximum amount of disorder caused by doping. In this series, the specimens with 5.1 and 9.3 at. % tin show preferred orientation along the $[111]$ axis. In the specimen with

TABLE II. Average grain radius (nm) as a function of tin concentration.

Tin concentration (at. %)	Normal specimens	Zone-confined specimens
4.2	47.3 ± 0.7	17.3 ± 0.6
5.1	33.4 ± 0.8	23.3 ± 0.8
6.6	17.4 ± 0.7	12.6 ± 0.7
9.3	27.6 ± 0.8	18.4 ± 0.7

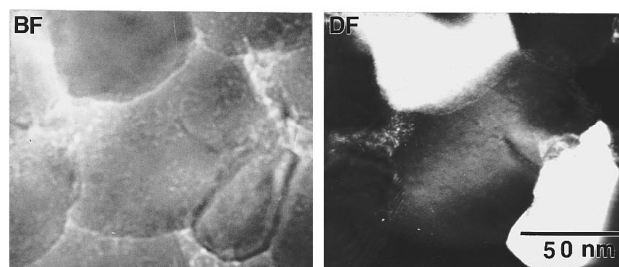


FIG. 3. Bright- and dark-field image from the same grain in a specimen with 9.3 at. % tin showing dopant clusters on the grain surface.

TABLE III. Texture coefficient for different sets of planes as a function of dopant concentration C_{Sn} for the specimens prepared with zone-confining arrangement.

C_{Sn} (at. %)	No. of peaks	Texture coefficients						
		{211}	{222}	{400}	{411}	{431}	{440}	{622}
4.2	31	1.66	1.66	1.64	1.31	1.29	1.40	1.15
5.1	25	1.51	2.58	1.38	0.92	1.35	1.07	1.03
6.6	18	1.61	2.05	2.10	1.23	0.79	0.85	0.98
9.3	27	1.36	2.57	0.46	0.59	1.38	1.51	1.37

4.2 at. % tin an equal fraction of grains has {211}, {222}, and {400} planes parallel to the film surface. The specimen with 6.6 at. % tin shows preferred orientation along the [100] axis. Previously, preferred orientation along the [100] and the [111] axes has been reported for both pure and tin-doped indium oxide films.¹⁰

Figure 4 shows that SAED patterns from the specimens in this series are consistent with the indium oxide bcc bixbyite structure; however, four extra rings corresponding to {110}, {200}, {220}, and {310} forbidden reflections are observed. These reflections have previously been observed but not explained in electron-diffraction patterns by Hamberg and Granqvist.⁶ Reflections corresponding to {200} and {220} planes have been observed by x-ray diffraction from single crystals.¹¹ Although allowed and forbidden reflections in the reciprocal lattice are given on the basis of kinematical diffraction theory by the structure factor, certain forbidden reflections can occur in electron-diffraction patterns due to double diffraction.¹² Forbidden reflections observed by x-ray diffraction of single crystals¹¹ might have been generated by stacking faults. The only diffraction pattern which shows a distinct diffuse ring is from the specimen with 6.6 at. % tin concentration [Fig. 4(c)].

Table II shows the average grain radius calculated for zone-confined specimens. Dark-field images from the specimens in this series (Fig. 5) show that, apart from the specimen with 5.1 at. % tin [Fig. 5(b)], all specimens have a

highly disordered intergranular phase. To verify the noncrystalline character of this phase, images were recorded with the objective aperture at six different positions around the ring corresponding to {222} planes. These images were identical within statistical limits,¹³ consistent with the idea that the intergranular regions were amorphous. All specimens which show an intergranular amorphous phase show strongly faceted crystalline grains. Although the specimen with 5.1 at. % tin [Fig. 5(b)] showed no intergranular amorphous phase, a few faceted grains could be seen. In the specimens with large areas of intergranular amorphous phase, crystallites grow in long chains with similar orientation following the lines of equal temperature on the substrate [Figs. 5(a) and 5(c)]. These chains are also observed in the images of the specimens with no or very little intergranular amorphous phase [Figs. 5(b) and 5(d)]. Some highly disordered or deformed grains similar to those seen in Figs. 2(c) and 2(d) are seen in all specimens in this series.

In general, specimens containing both intergranular amorphous and crystalline phases were highly disordered; even crystalline grains observed in these specimens seemed to have high defect densities. However, individual point and linear defects could not be identified. Figure 6 shows a stacking of (112) planes in faulted (110) planes in the specimen with 6.6 at. % tin; the electron beam is parallel to (110). This is consistent with Nabarro's¹⁴ suggestion for the occurrence of stacking faults on (112) or (110) planes in bcc crystals. Small clusters are observed with fringes (~ 0.3 nm) running in a completely different direction to the matrix as marked by circles in Fig. 6. These clusters could not be identified as stacking faults and thus may be related to impurity segregation. Polycrystalline specimens having optimum electrical and optical properties showed highly ordered grains. Grain boundaries between two adjacent zones or chains were either high-angle tilt, overlapping low-angle tilt, or twist boundaries. Figure 7 shows three grains marked A, B, and C appearing in one region of the specimen with 5.1 at. % tin. The boundary between grains A and B is a twist boundary obtained by a rotation of 45° about the $[1\bar{1}1]$ axis. The boundary between grains B and C is also a twist boundary obtained by a rotation of 90° about the $[101]$ axis. Figure 8 shows another set of three grains appearing in another region of the same specimen. Grain A shows fringes with a spacing of 0.42 nm which correspond to the {211} planes of bcc indium oxide while grains B and C show fringes with a spacing of 0.39 nm which correspond to the {021} planes of the hexagonal phase of indium oxide. Grains B and C are separated by a $(22\bar{1})$ twin. It was very difficult to determine the exact

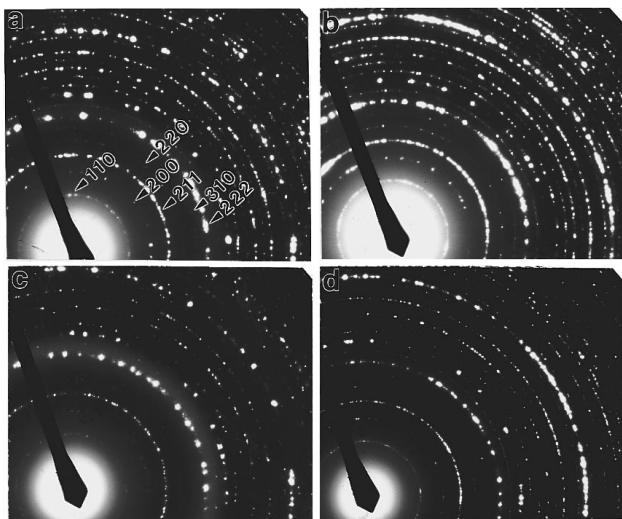


FIG. 4. SAED patterns from specimens prepared with zone-confining arrangement with dopant concentrations of (a) 4.2, (b) 5.1, (c) 6.6, and (d) 9.3 at. %.

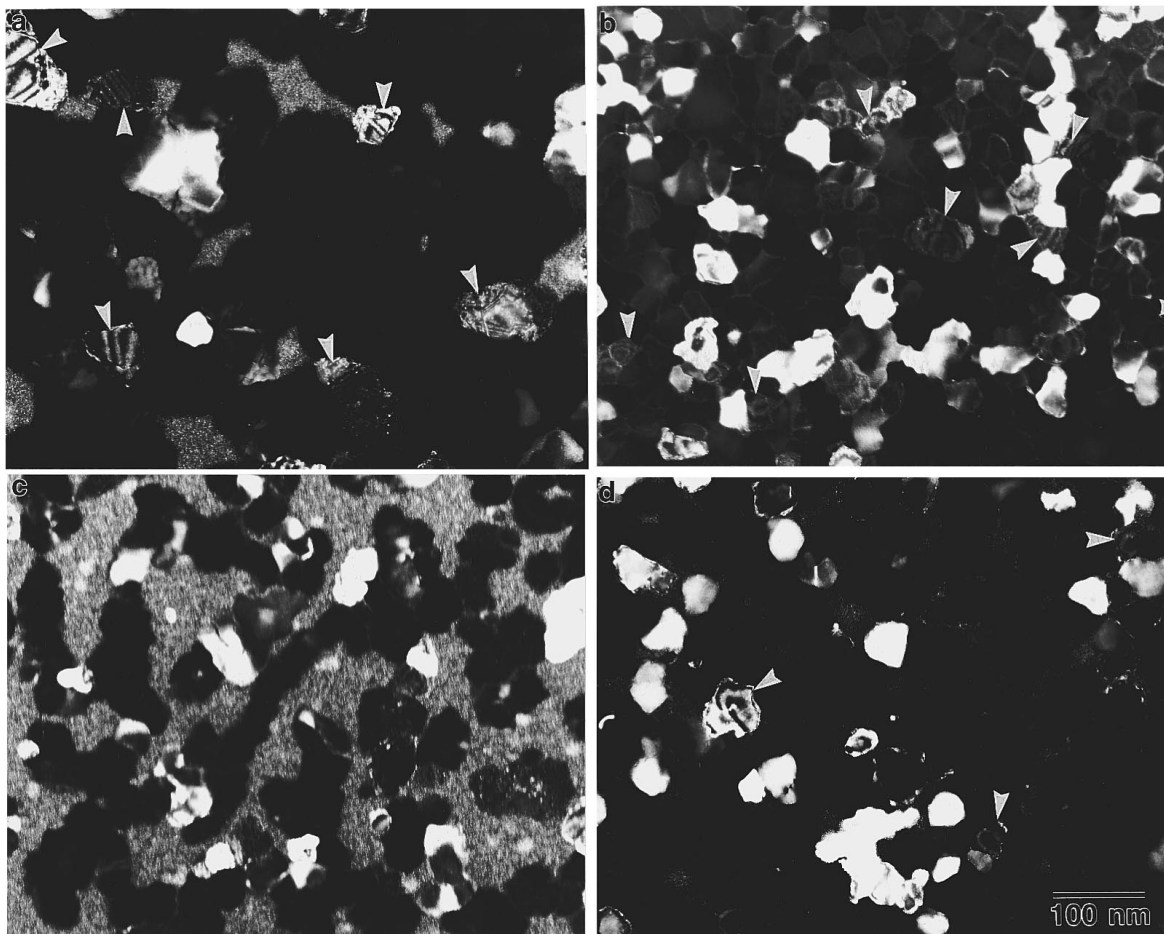


FIG. 5. Dark-field images from the specimen prepared with zone-confining arrangement with a dopant concentration of (a) 4.2, (b) 5.1, (c) 6.6, and (d) 9.3 at. %.

position of the regions imaged by Figs. 7 and 8, relative to the heating element. It is suspected that the grains seen in Fig. 8 were closer to the heating element and grew under a sharper temperature gradient, thus producing a more pronounced zone-confining effect and a twin or relaxed grain boundary (boundary between hexagonal and bcc phases). Those seen in Fig. 7 grew in a region farther from the heating element where the temperature gradient was more moderate and generated near-coincidence lattice site boundaries instead of twins. This hypothesis has been confirmed for chemical-vapor-deposited Cu films.¹⁵

C. Recrystallization of the intergranular amorphous phase

Films with a large area of intergranular amorphous phase were best suited to study the electron-beam recrystallization mechanism *in situ* using TEM. It is known that the amorphous phase of indium oxide does not follow a typical nucleation and growth process for crystallization but gradually improves in order over the whole area of a particle.¹⁶ In the biphasic specimens under discussion, the amorphous phase is perhaps already in a higher-energy state so the initial ordering process in these regions is very fast and extremely difficult to image; however, some good images which provide evidence for the recrystallization process were recorded.

Figure 9(a) shows an image recorded just after the initial stage of ordering in the amorphous phase. Regions marked A represent the original crystalline grains in the film, while regions marked B are those recrystallized from grains

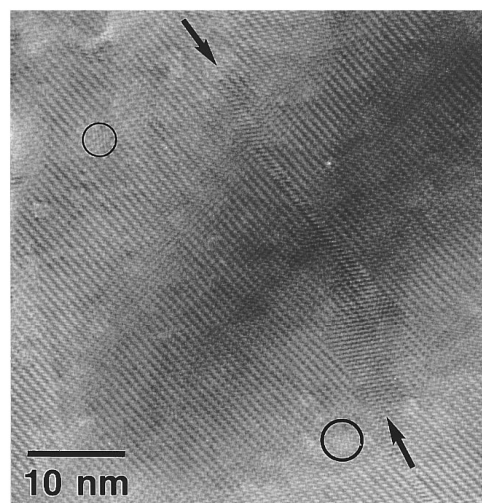


FIG. 6. A high-resolution image showing a stacking of (112) planes in (110) planes of bcc indium oxide (marked by arrows) and fringes with 0.3 nm spacing (marked by circles).

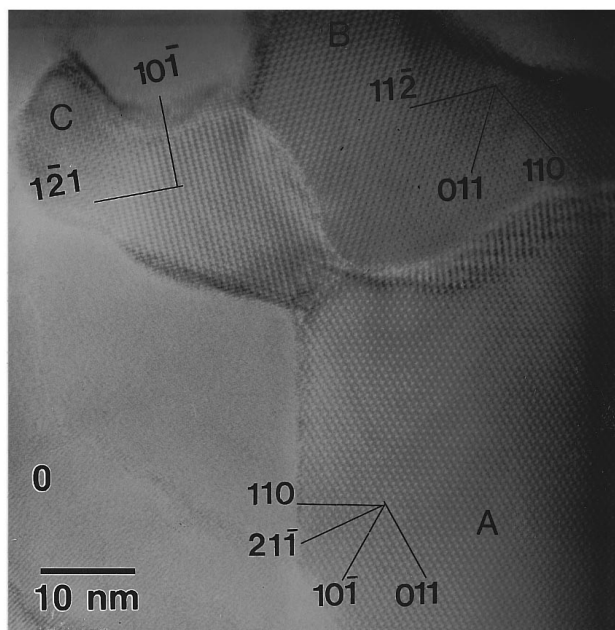


FIG. 7. A high-resolution lattice image showing three grains oriented in the same direction forming twist boundaries.

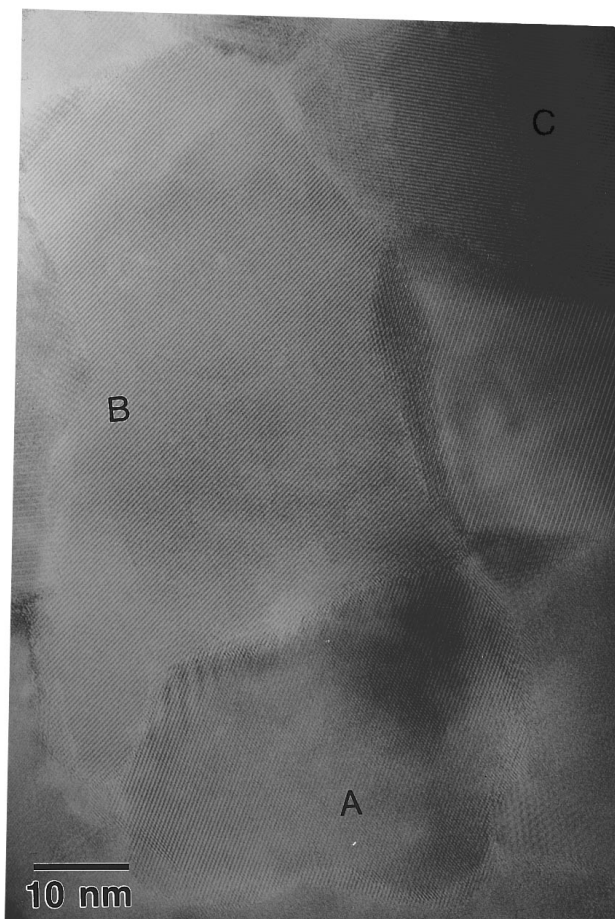


FIG. 8. A high-resolution lattice image showing a twin between (021) and (102) planes of hexagonal phase of indium oxide (grains B and C) and a boundary between (021) planes of hexagonal and (211) planes of cubic indium oxide (grains B and A, respectively).

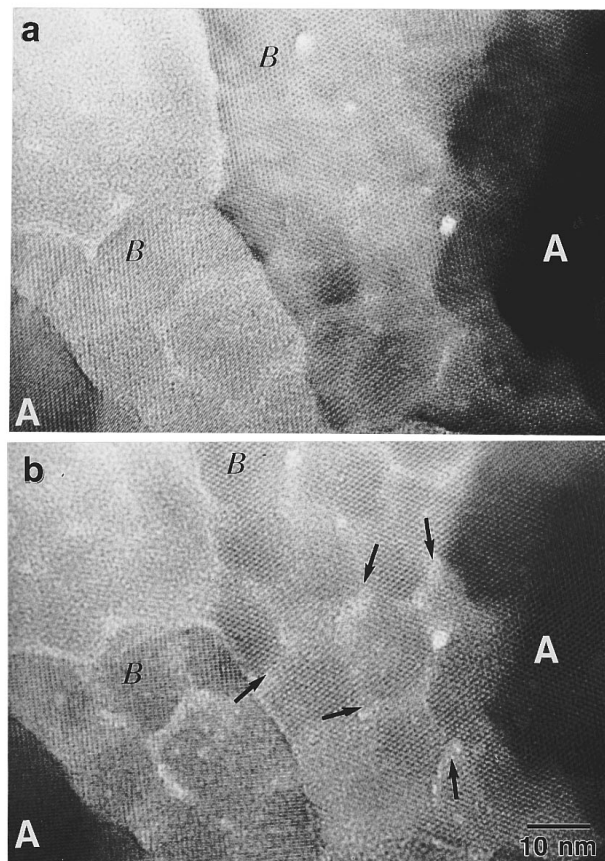


FIG. 9. A high-resolution image showing the growth of new, highly ordered grains by annealing the defects out to boundaries.

marked A. Figure 9(b) represents the same area after 2 min of electron-beam irradiation. By comparing Fig. 9(b) with Fig. 9(a), it is seen that a particulate structure of highly ordered regions develops and regions marked with arrows become highly disordered. This is interpreted as the formation of highly ordered new nuclei for recrystallization by annealing out of defects into the boundaries separating those nuclei.

D. Electrical properties

The achievement of the lowest possible resistivity is of practical significance because it provides some freedom in selecting the film thickness to achieve high optical transmission while still maintaining low sheet resistance. The lowest resistivity reported for ITO films is of the order of $1.6 \times 10^{-6} \Omega \text{ m}$.¹⁷ In the present work, sheet resistances for film thicknesses between 82 and 1200 nm varied between 1.9 and 17.6 Ω/\square . Table IV shows the measured dc resistivity as a function of dopant concentration. The specimen with 5.1 at. % tin prepared under zone-confining arrangements showed the best value of $4.4 \times 10^{-7} \Omega \text{ m}$. This is a factor of ~ 4 better than the best resistivity reported.¹⁷ In both series, the specimen with 6.6 at. % tin shows the highest value of resistivity. This specimen had the maximum amount of intergranular amorphous phase which is likely responsible for the high resistivity.

Table V shows the computed free carrier density for all specimens. For normally prepared specimens, the carrier

TABLE IV. Measured dc resistivity $\rho \times 10^{-6}$ (Ω m) as a function of dopant concentration.

Tin concentration (at. %)	Normal specimens	Zone-confined specimens
4.2	1.7	1.2
5.1	6.8	0.44
6.6	9.1	3.4
9.3	4.8	1.9

density is the highest at a tin concentration of 4.2 at. % and decreases with increasing dopant concentration up to 6.6 at. %. It increases again when the tin concentration is increased to 9.3 at. %. For zone-confined specimens the carrier density increases when the tin concentration is increased from 4.2 to 5.1 at. %, decreases when the tin concentration is increased to 6.6 at. %, and increase again for 9.3 at. % tin. Table VI shows the conduction mobilities as a function of dopant concentration. The dc conduction mobilities for zone-confined specimens are considerably higher than those for normal specimens. In both cases the mobility is lowest for specimens with 6.6 at. % Sn. Assuming a free electron model, the mean free path of the electrons is given as¹⁸

$$l = (3\pi^2)^{1/3} \frac{h}{\rho e^2 n^{2/3}}, \quad (2)$$

where ρ is the resistivity and n is free carrier density. Table VII shows the mean free path for the specimens prepared with different dopant concentrations in both series. The mean free path correlates closely with the grain size for the normal specimens, and is much larger compared to the grain size for zone-confined specimens.

IV. DISCUSSION

A. Microstructure

In order to understand the growth kinetics of films deposited at high substrate temperatures it is useful to divide the whole growth process into two major steps:

- (1) formation of the first layer of the films by collision of incoming vapor with the substrate, transfer of the kinetic energy of the vapor to the substrate, and condensation of the vapor to the solid phase;
- (2) deposition of the second layer in the same way except that energy is transferred to the layer which has already deposited.

TABLE V. Carrier density $n \times 10^{26}$ (m^{-3}) as a function of dopant concentration.

Tin concentration (at. %)	Normal specimens	Zone-confined specimens
4.2	9.8	9.5
5.1	5.7	13.8
6.6	5.6	6.5
9.3	7.0	7.6

TABLE VI. Calculated dc conduction mobilities μ_c ($\text{m}^2/\text{V s}$) as a function of dopant concentration.

Tin concentration (at. %)	Normal specimens	Zone-confined specimens
4.2	0.0038	0.0055
5.1	0.0016	0.0103
6.6	0.0012	0.0028
9.3	0.0019	0.0043

After deposition of the second layer the surface mobility of the first layer is reduced and the structure grows as tapered crystallites from the first layer into the second and so on;¹⁹ however, for continuous film deposition the kinetic energy of the incoming vapor, which is transferred in the form of heat to the top layer, is conducted through the grown layers to the substrate. In the case of high substrate temperatures this conduction process is slow and might active recrystallization in the layers grown already. This is likely to occur in the present case because of the exceptionally slow deposition rates. Strain-free structures are thus expected to develop during deposition.

Section III A suggests that crystallization of the intergranular amorphous phase proceeds in two steps:

- (i) rapid growth of neighboring grains into the amorphous phase to form highly disordered grains;
- (ii) formation of highly ordered crystallites by annealing the defects out to boundaries.

This suggests that ordered grains are a consequence of defect segregation. These defects include stacking faults, dislocations, impurity atoms, and oxygen vacancies. The appearance of an intergranular amorphous phase in the specimen prepared with 6.6 at. % Sn under normal conditions can be explained as a consequence of dopant as well as defect segregation. When the dopant concentration exceeds the solid solubility limit (5 at. % Sn), the dopant cannot remain in solid solution and is pushed out toward the boundaries. In some of the intergranular regions the dopant concentration becomes so high that it cannot retain the host (indium oxide) bixbyite bcc rare-earth structure and has a tendency to adopt its own rutile (SnO_2) structure. These regions are surrounded by host grains which exert epitaxial pressure forcing them to amorphize in an effort to regain their natural structure. This is seen in many epitaxial heterostructures before the material regains its natural structure. Disappearance of such regions in specimens with 9.3 at. % Sn is explained by segregation of

TABLE VII. Mean free path (nm) calculated from the experimental data using the free electron model.

Tin concentration (at. %)	Normal specimens	Zone-confined specimens
4.2	48	69
5.1	17	147
6.6	13	31
9.3	21	51

the dopant to the surface of the grains.³ Because of the migration of defects toward the grain boundaries, the defect density over the boundary will increase thereby increasing the grain-boundary volume which will exert a force on each grain, deforming some of them.

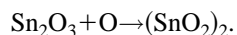
For zone-confined specimens this tendency to anneal defects toward grain boundaries is coupled with exceptionally slow deposition rates. A driving force similar to zone refining is provided through the temperature gradient. For two adjacent lines of crystallites which grow at different temperatures, defects and dopants within a zone of crystallites growing on a line of lower temperature will have a lower solubility than in those at higher temperature. Hence, the dopant and defects from the zone of crystallites growing at a lower temperature migrate from that zone and are confined in the boundaries or intergranular regions between this zone and the next zone. The initial zone-confining effect is simultaneously assisted by recrystallization due to exceptionally slow deposition rates. Grains within a zone are oriented in the same direction and boundaries separating them are twin boundaries or are of the type which are very relaxed and cause the least amount of scattering to mobile electron (boundary between hexagonal and bcc grains²⁰). Due to this reorganization the zone-confining process not only produces preferred orientation at the desired position, but also causes the selective boundaries to be twin boundaries. This is an important process for fabricating materials which have higher electron mobility along certain crystalline planes.

B. Free carriers

For normally prepared specimens, the sample with 4.2 at. % Sn produces the highest number of free carriers with all other samples in this series having smaller values. For zone-confined samples, 5.1 at. % Sn produces the highest number of free electrons and the lowest value of electrical resistivity. This is the only specimen in this series which did not show an intergranular amorphous phase.

Kostlin, Jost, and Lems²¹ have studied the effects of tin concentration on the carrier density of tin-doped indium oxide films prepared by a pyrolytic method at a substrate temperature of 500 °C under normal atmospheric conditions. The carrier density increased with increasing tin concentration up to 8 at. % tin but decreased for higher tin contents. They presented two arguments to explain the decrease in the carrier density above the optimum tin concentration, as follows:

- (1) When two tin atoms substitutionally replace two neighboring indium atoms, one of these atoms changes its valency from 4+ to 2+ so that a neutral complex $\text{Sn}^{2+}-\text{Sn}^{4+}$ is formed with respect to the normal matrix.
- (2) The tin pair substitutionally replacing two neighboring indium atoms strongly binds an additional oxygen to form a neutral complex which consists of two Sn^{4+} and the additional oxygen, that is,



They rejected the first possibility on the basis of Mössbauer spectroscopy because they could not detect any diva-

lent tin cations at any tin concentration. In the present case exceptionally slow deposition rates as well as very low partial pressures of oxygen were used for depositing all specimens. The deposition rates as well as recrystallization in the growing grains encourage the segregation of tin atoms toward the grain boundaries. Simultaneously the segregation of other defects (i.e., oxygen vacancies) toward the boundaries is encouraged. Thus in the segregated state, if the tin atoms tend to form an $(\text{SnO}_2)_2$ complex, this will be discouraged by the deficiency of oxygen over the boundaries. Tin atoms in a segregated state may have a natural tendency to adopt the tetragonal SnO_2 structure since this is the most stable phase of tin oxide; however, in this case they are forced to adopt the host bixbyite rare-earth bcc structure. Due to lattice mismatch a highly disordered $\text{Sn}_2\text{O}_{3-x}$ or in some cases, depending on the concentration of dopant in the segregated state, an amorphous $\text{Sn}_2\text{O}_{3-x}$ structure may result. This amorphous phase, if caused by the epitaxial effects of the neighboring grains, would be expected to become increasingly disordered away from the grain boundaries. This was the case for our specimens.²² Although the formation of the $(\text{SnO}_2)_2$ complex will be least probable in the present case due to amorphization of the segregated $\text{Sn}_2\text{O}_{3-x}$ phase, there will be a large number of trap states for free electrons. Although each tin atom present will contribute one electron, these will be trapped and will not contribute to the free carrier density. This is likely to be true since the specimen which has the highest value of carrier density does not show any intergranular amorphous phase.

Correlation of the mean free path with the grain size for specimens prepared under uniform temperature indicates that the electrons travel through a distance equal to the average size of the grain before being scattered. In the case of zone-confined specimens this distance is much larger than the average grain size. For the best specimen, the distance is four times the average size of the grains indicating that the electrons remain unscattered when they come across a grain boundary (which usually is twinned) between grains grown on the same line of equal temperature. This also indicates that the four times improvement in the resistivity is primarily due to the improvement in the distance electrons can travel before being scattered. This is a consequence of the zone-confining process.

V. CONCLUSIONS

(1) Indium oxide has a tendency to form highly ordered crystallites by the migration of defects including dopant atoms toward grain boundaries. As a consequence of the increased dopant concentration, large areas of an intergranular amorphous phase are produced at a tin concentration of 6.6 at. %. At larger tin concentrations segregation of dopant occurs toward the surface of the grains.

(2) Because of the segregation of dopants and other defects toward the grain boundaries, the grain-boundary volume increases and a pressure is exerted upon each of the neighboring grains such that some grains are deformed.

(3) The zone-confining process coupled with slow deposition rates causes preferential segregation of dopants from grains growing at lower temperature toward the boundaries

appearing at higher temperature. Simultaneously a recrystallization process within the zones of grains growing on the same line of equal temperature orients these grains in the same direction with respect to the substrate, and the boundaries separating two such grains are twin boundaries.

(4) Under zone-confining arrangements, a 5.1 at. % tin concentration produces optimum electrical properties.

(5) In zone-confined specimens, electrons travel at least twice the average size of the grains. Under optimum conditions, this distance is four times the average grain size. For specimens with optimum properties each zone contains an average of four grains separated by a dopant free twin boundary.

¹K. L. Chopra, S. Major, and D. K. Pandya, *Thin Solid Films* **102**, 1 (1983).

²I. A. Rauf, M. G. Walls, and P. H. Gaskell, *Trans. R. Microsc. Soc.* **1**, 165 (1990).

³I. A. Rauf, in *Proceedings of the 12th International Congress for Electron Microscopy*, Seattle, WA, edited by L. D. Peachey and D. B. Williams (San Francisco Press, San Francisco, 1990), Vol. 4, p. 716.

⁴I. A. Rauf, *J. Mater. Sci. Lett.* **12**, 1902 (1993).

⁵I. A. Rauf, *Mater. Lett.* **18**, 123 (1993).

⁶I. Hamberg and C. G. Granqvist, *J. Appl. Phys.* **60**, R123 (1986).

⁷L. J. Van der Pauw, *Phillips Res. Rep.* **13**, 1 (1958).

⁸I. A. Rauf, *Mater. Lett.* **23**, 73 (1995).

⁹H. K. Kim and J. S. Chun, *Thin Solid Films* **141**, 287 (1986).

¹⁰P. Nath, R. F. Bunshah, B. M. Basol, and O. M. Staffsud, *Thin Solid Films* **72**, 463 (1980).

¹¹M. Marezio, *Acta Crystallogr.* **20**, 273 (1966).

¹²P. Hirsh, A. Howie, R. B. Nicholson, D. W. Pashley, and M. J. Whelan, *Electron Microscopy of Thin Crystals* (Robert E. Krieger, New York, 1977), p. 117.

¹³I. A. Rauf and J. Yuan, *Mater. Lett.* **25**, 217 (1995).

¹⁴F. R. N. Nabarro, *Theory of Crystal Dislocations* (Oxford University Press, London, 1967), p. 210.

¹⁵I. A. Rauf, L. Weaver, E. Griswold, P. N. Gadgil, M. Sayer, and J. D. Boyd (unpublished).

¹⁶I. A. Rauf and L. M. Brown, *Acta Metall. Mater.* **42**, 57 (1994).

¹⁷L. A. Ryabova, V. S. Salun, and I. A. Serbinov, *Thin Solid Films* **92**, 327 (1982).

¹⁸Hoffmann, J. Pickl, M. Schmidt, and D. Krause, *Appl. Phys.* **16**, 239 (1978).

¹⁹R. F. Bunshah and C. Deshpandya, in *Physics of Thin Films*, edited by M. H. Francombe and J. L. Vossen (Academic, London, 1987), p. 59.

²⁰C. Yuanri, X. Xinghao, J. Zhaoting, P. Chuancai, and X. Shuyun, *Thin Solid Films* **115**, 195 (1984).

²¹H. Kostlin, R. Jost, and W. Lems, *Phys. Status Solidi A* **29**, 87 (1975).

²²I. A. Rauf and M. G. Walls, *Ultramicroscopy* **35**, 19 (1991).